RESEARCH ARTICLE

ADVANCED MATERIALS INTERFACES
Open Access
www.advmatinterfaces.de

The Impact of Gas Cluster Ion Beam Sputtering on the Chemical and Electronic Structure of Methyl Ammonium Lead Iodide Thin Films

*Emily Albert, Fengshuo Zu, Dongguen Shin, Patrick Amsalem, and Norbert Koch**

The stability and performance of metal halide perovskite (MHP) optoelectronic devices are significantly influenced by the chemical and electronic properties of their interfaces, often studied using photoelectron spectroscopy (PES). MHP films, containing organic cations, are susceptible to surface modifications under common experimental conditions, necessitating careful analysis. This study examines the effects of argon gas cluster ion beam (GCIB) sputtering, considered gentler and more suitable for depth-profiling than standard argon ion sputtering, on methylammonium lead iodide using PES. Long-term exposure to argon clusters with 3.2 and 1.5 eV per Ar atom causes significant degradation, including cation loss and metallic lead formation. However, short-term exposure (<60 min) at 1.5 eV per Ar atom effectively reduces surface contamination without noticeable degradation, allowing access to intrinsic electronic properties. This gentle cleaning reveals a 220 meV energy difference between the contaminated surface and the valence band onset of the intrinsic MHP potentially improving energy level alignment with electron transport layers. These results demonstrate that low energy GCIB sputtering can serve as a non-destructive surface cleaning method, enhancing PES investigations and supporting fundamental device studies of MHPs.

1. Introduction

Metal halide perovskites (MHP's) have attracted significant attention due to their excellent optoelectronic properties,[1–5] making them promising candidates for a range of optoelectronic devices.[6–8] The performance and stability of MHP-based devices are largely influenced by their chemical and electronic properties at surfaces and interfaces. Thus understanding the surface and interface electronic properties of MHPs is fundamental for further advancing their applications, e.g., in photovoltaics.[9–11] For instance, high-performance MHP solar cells require proper energy level matching between the perovskite and charge transport layers,[12] which can be significantly altered by the presence of surface states.[13] In addition, the interfacial recombination, being a surface mediated energy loss process,[14] is directly related to the density of gap states. These imperfections at the surface of MHPs can be associated with interstitials and vacancies in the lattice or grain boundaries terminating the surface.[15,16] Chemical surface treatments like molecular modification have been employed to mitigate these challenges by passivating defects and enhancing material stability.[17,18] However, these treatments often introduce additional complexity, such as scalability as well as reliability issues and the risk of a different chemical passivator for each perovskite composition. Consequently, there is an increasing interest in non-chemical surface treatments such as laser polishing and plasma exposure. These methods offer scalable solutions for surface defect passivation, improved crystallinity, and enhanced efficiency in solar cell devices, without the disadvantages associated with chemical methods.[19–22] To unravel the surface and interface electronic properties of MHPs, photoelectron spectroscopy (PES) has been widely used,[23–25] and can provide detailed insights into the electronic structure, elemental composition, and chemical states at the surface. For instance, X-ray photoelectron spectroscopy (XPS) is commonly applied to investigate the chemical state information, whereas ultraviolet photoelectron spectroscopy (UPS) probes the valence electronic structure

E. Albert, F. Zu, D. Shin, P. Amsalem, N. Koch
Institut für Physik & IRIS Adlershof
Humboldt-Universität zu Berlin
12489 Berlin, Germany
E-mail: norbert.koch@physik.hu-berlin.de

E. Albert, F. Zu, N. Koch
Helmholtz-Zentrum Berlin für Materialien und Energie GmbH
12489 Berlin, Germany

D. Shin
Department of Physics
Chonnam National University
Yongbong-ro 77, Buk-gu, Gwangju 61186, South Korea

The ORCID identification number(s) for the author(s) of this article can be found under https://doi.org/10.1002/admi.202500102

DOI: 10.1002/admi.202500102

and the work function. With both PES variations being surface sensitive due to the short inelastic mean free path (IMFP) of the photoelectrons, UPS is even more surface sensitive than XPS given the lower kinetic energy of photoelectrons (ca. 10 – 20 eV), thus extracting the bulk valence band of the material becomes very challenging. This limitation can potentially be overcome by combining PES with the use of gas cluster ion beam (GCIB) sputtering. GCIB sputtering is an advanced technique used in materials science for surface cleaning, modification, and depth-profiling analysis. Unlike traditional ion beam sputtering, which uses single ions, GCIB employs clusters of gas atoms, typically noble gases like argon, that are ionized and accelerated toward the target material. The impact of the gas clusters results in a unique sputtering mechanism where the energy is distributed across thousands of atoms, reducing the risk of damaging the sample surface. This comparably gentle sputtering process is ideal for applications requiring high precision and minimal damage to the target surface, thus constituting a non-chemical surface cleaning and depth-profiling possibility for sensitive materials.[26–28] In combination with UPS measurements, GCIB sputtering has been suggested effective in probing the evolution of energy levels across device layer stacks for organic light emitting diodes (OLEDs),[29] as well as across buried perovskite interfaces[30] and perovskite photovoltaic devices.[31,32] However, available MHP-related studies focused on depth-profiling did not critically look at potential degradation when using GCIB, thus leaving information reliability an open question.

In this contribution, we examined the impact of both long-term (as needed for depth-profiling) and short-term (as used for surface cleaning) exposure to argon clusters on the surface electronic and chemical properties of the archetypal methylammonium lead iodide ($MAPbI_3$). For the purpose of depth profiling, we observed clear degradation for two different kinetic energies of Ar clusters, i.e., 3.2 and 1.5 eV per argon atom (eV/Ar), respectively. Notably, sputtering under 3.2 eV/Ar already results in degradation after 1 h, corresponding to a sputter depth of only a few nm, with the formation of a substantial amount of metallic lead. On the other hand, short time exposure (< 60 min) to 1.5 eV/Ar clusters shows a significant reduction of carbon contamination and surface iodine without notable sample degradation, indicating a successful application of GCIB for the purpose of surface cleaning. Such a damage-free surface cleaning process helps reveal the intrinsic surface electronic properties and allows to measure the intrinsic/ideal energy offset at perovskite/charge transport layer interfaces.

2. Results and Discussion

2.1. GCIB Employed as Depth Profiling

To understand the occurrence of energy losses in devices, non-destructive characterization of energy level alignment at interfaces,[9,33] is crucial, but probing the energy level alignment at buried interfaces is especially challenging. This becomes particularly demanding when the interface involves metal halide perovskites because of their sensitivity to external stimuli.[34–38] With the emergence of GCIB for depth profiling, numerous studies utilized this technique to reach the buried interfaces, however, its impact on the chemical and electronic structure of the material is still under debate.[26,30–32]

Utilizing the archetypical $MAPbI_3$, we investigated the impact of argon clusters on the electronic (UPS) and chemical (XPS) properties of the perovskite surface by sputtering $MAPbI_3$ films under two cluster settings. The Ar cluster size distribution as a function of kinetic energy is shown in supplementary Figure S1 (Supporting Information). The peak maximum of the distribution is taken to determine the kinetic energies per argon atom (E_{kin}/Ar) value and a broadening of the Ar cluster size distribution is noted.

Here, 3.2 and 1.5 eV/Ar are employed for incremental sputtering, with 1.5 eV/Ar delivering the lowest kinetic energy of the argon clusters by the GCIB system. The valence band onset and work function (WF) values were graphically determined by linear extrapolation of the photoelectron intensity axis toward the background line, i.e., by identifying the intersection between the background line and a tangent drawn at the point of maximum slope of the top of the valence band and the secondary electron cutoff (SECO). An example is shown in Figure S2 (Supporting Information).

The results for sputtering with settings at 3.2 and 1.5 eV/Ar are summarized in **Figure 1**. For 3.2 eV/Ar, Figure 1a shows a tremendous shift of the WF by $\Delta WF = 1.0$ eV as determined from the SECO after 16 h of sputtering, accompanied by a slight change in the feature of the valence band, as shown in Figure 1b. We identify the formation of elementary lead (Pb^0) already after 1 h of sputtering, which clearly evidences the degradation of $MAPbI_3$, as shown in Figure 1c. In contrast, no Pb^0 is detected in the first 16 h under 1.5 eV/Ar, indicating a significantly reduced degradation when employing a lower E_{kin}/Ar. Another indicator for Pb^0 is the appearance of a Fermi edge at $E_F = 0$ eV binding energy (BE), clearly visible after 32 h of sputtering under 3.2 eV/Ar presented in Figure S3 (Supporting Information). Although we observe a substantial amount of metallic Pb from Pb 4f core levels already after 13 h sputtering at 3.2 eV/Ar, the corresponding valence band does not clearly exhibit the emergence of Fermi edge, likely due to the low signal-to-noise ratio. Since the increasing concentration of Pb^0 leads to the formation of additional states close to the VB onset and therefore inaccuracies in the VB onset determination, we refrain from giving IE values.[39,40]

The degradation process of $MAPbI_3$ can be generally described as: $MAPbI_3 + P_{ext} \rightarrow PbI_2 + I^- + MA^+$, where P_{ext} denotes the external stimuli such as irradiation,[37,39] humidity,[41,42] or oxygen.[42] Upon illumination, PbI_2 further decomposes into Pb^0 and gaseous I_2 due to photolysis.[36,39] Using 3.2 eV/Ar we observed a complete loss of carbon and nitrogen on the surface after 1 h of sputtering, in agreement with the emergence of the Pb^0 core level. In accordance with the increased formation of Pb^0, we see a significant reduction of iodine with advancing sputter time t_{GCIB}, as shown in the atomic ratio of I/Pb in Figure 1e, indicating the formation of PbI_2. From the first hour and up to 16 h of sputtering, $MAPbI_3$ gradually degrades into PbI_2 and metallic Pb while the valence band still represents the perovskite feature, indicating a partial degradation on the surface. As the surface stoichiometry evolved due to degradation, corresponding shifts in the electronic structure, evidenced by changes in the SECO and VB onsets, were detected and anticipated. After 13 h we also observe a shift in the Pb 4f core levels in Figure 1c. Continued

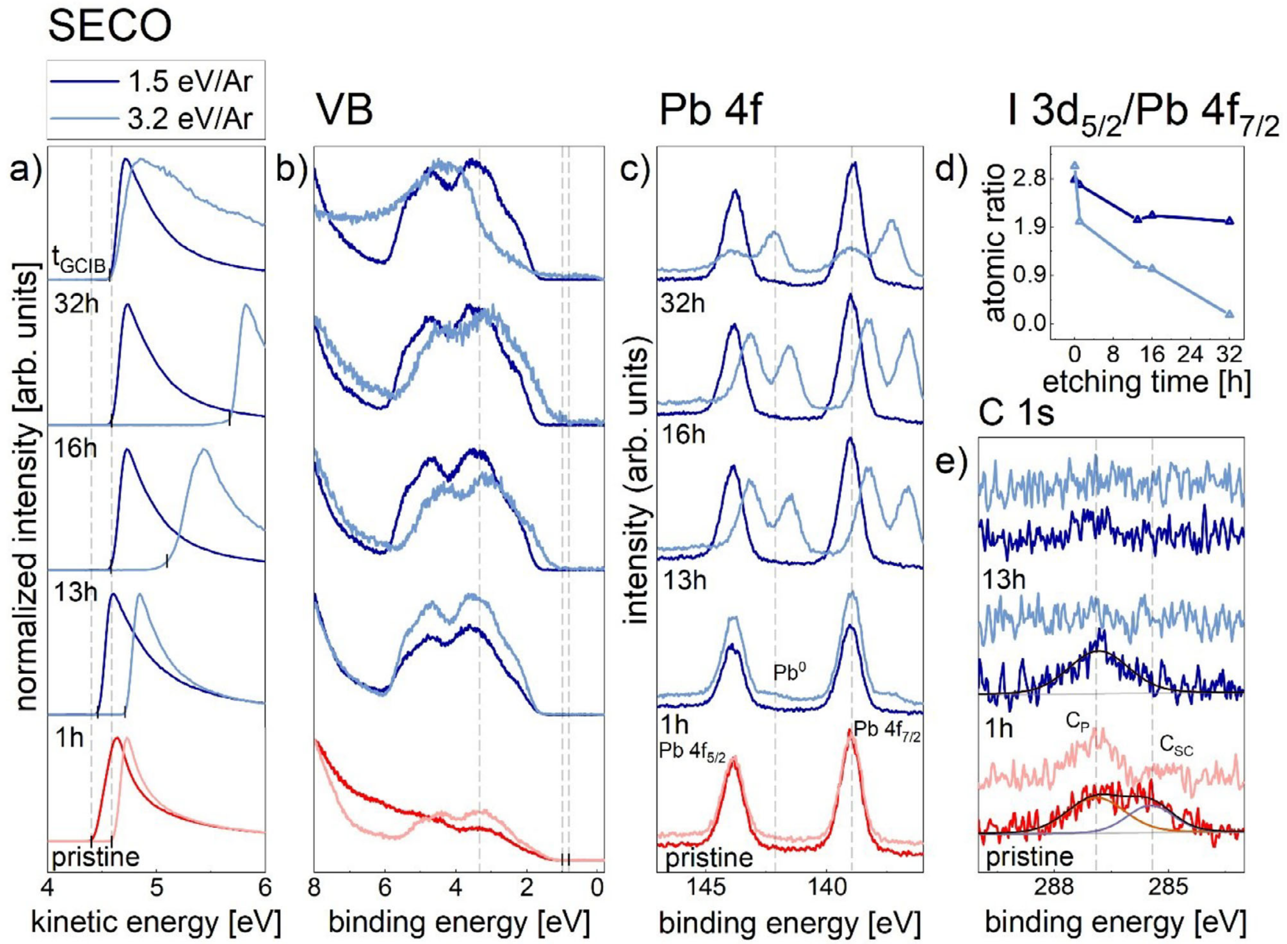

Figure 1. **Figure 1**. Impact of using argon clusters of 1.5 eV/Ar (dark line) and 3.2 eV/Ar (bright line) for depth profiling on the chemical and electronic properties of $MAPbI_3$. All pristine spectra a shown in red while the exposure to GCIB is shown in blue. The evolution of a) the SECO, b) the valence band, c) Pb 4f, e) C 1s, and d) the atomic ratio of iodine to lead as a function of sputtering time. The dotted lines in a), b), c), and d) indicate the work function, the VB onset and main feature, the peak position of Pb $4f_{5/2}$ and Pb $4f_{7/2}$ as well as C_P and C_{SC} of the pristine film, respectively.

sputtering after 16 h drastically changed the surface composition where the metallic Pb dominates on the surface and the valence band differs significantly from the perovskite valence structure. We have refrained from discussing the shift of Pb 4f core levels, SECO and VB after 32 h sputtering as the sample mainly consists of metallic Pb (see Figure 1c) and traces of PbI_2 without any characteristic absorption features and almost no detected iodine (Figures S3 and S4, Supporting Information).

As for the cluster sputtering under 1.5 eV/Ar, a total shift of the work function by $\Delta WF = 0.2$ eV (Figure 1a) after $t_{GCIB} = 32$ h is observed. In addition, the valence band structure becomes more defined after $t_{GCIB} = 1$ h and remains unchanged thereafter. The chemical degradation of $MAPbI_3$, i.e., loss of iodine, carbon, and nitrogen is also observed but less severe than for 3.2 eV/Ar. Specifically, 1 h of 1.5 eV/Ar sputtering seems to remove the surface carbon-related contamination, while preserving the perovskite cation (MA^+) in the film. This is shown in Figure 1d and Figure S3 (Supporting Information) for the evolution of N 1s and C 1s as a function of t_{GCIB}, where the carbon peak at lower BE is commonly assigned to surface contamination (C_{SC}) (e.g., CH_3NH_2 species,[43,44]) and carbon peak at higher BE corresponds to perovskite cations (C_P). This also accounts for the observed change in the valence band structure after 1 h of sputtering under 1.5 eV/Ar. Further exposure to 1.5 eV/Ar ultimately results in the removal of the cation and iodine, as shown in Figure 1d and Figure S3 (Supporting Information) for I 3d and Figure 1e for C 1s, leading to the formation of PbI_2 on the surface.

The above observations unambiguously demonstrate that the cluster sputtering for depth-profiling experiments under both 3.2 and 1.5 eV/Ar ultimately degrades $MAPbI_3$. Using clusters of 1.5 eV/Ar is found to etch off ≈100 nm of $MAPbI_3$, giving rise to ca. 3 nm/h etching rate, while 3.2 eV/Ar is able to sputter through ca. 400 nm resulting in 12 nm/h etching rate (Figure S5, Supporting Information). Since there is most likely no linear dependency between the sputter depth and the sputtering time, foremost due to the chemical change of the perovskite, we refrain from giving a sputtered depth but rather provide the sputtering time for comparison.

Although the application of GCIB for the purpose of non-destructive depth profiling proves unattainable, it seems that 1.5 eV/Ar could potentially be employed as a non-damaging surface cleaning method. This can be seen from the

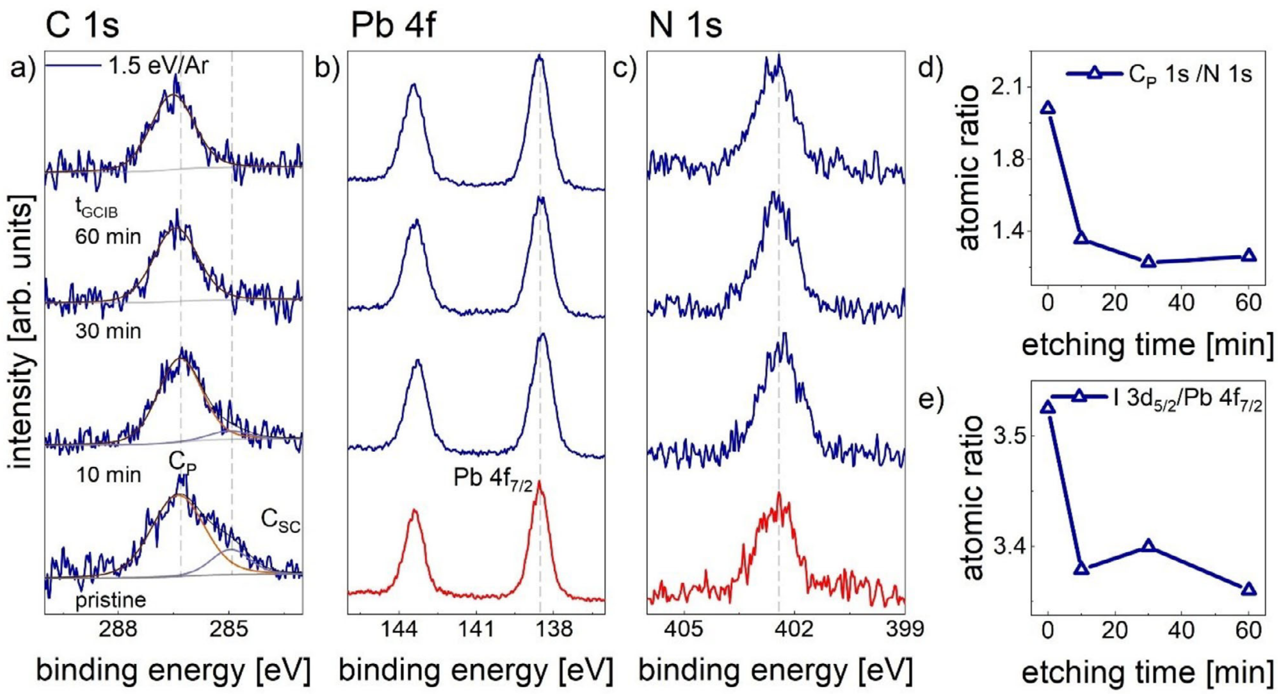

Figure 2. Evolution of core level spectra of a) C 1s, b) Pb 4f, c) N 1s, d) Cp to N 1s atomic ratio, and e) I to Pb atomic ratio as a function sputtering time under 1.5 eV/Ar. The dashed lines mark the peak positions for C_p 1s as well as C_{SC} 1s of the pristine film in a), the position of N 1s in c), and Pb 4f 7/2 in b).

significant reduction of the carbon contamination- related C_{SC} after 1 h of sputtering in Figure 1d, which likely accounts for the emergence of a more defined valence band structure upon sputtering.

2.2. GCIB Employed for Surface Cleaning

To assess whether GCIB can be employed as a non-destructive surface cleaning method, we conducted additional UPS and XPS measurements with a focus on the first hour of exposing $MAPbI_3$ to 1.5 eV/Ar.

In **Figure 2a**, we observe a clear reduction in C_{SC} after 10 min and the complete removal of C_{SC} after 30 min. Concomitantly, in Figure 2b the Pb 4f peaks remain unchanged and we do not detect Pb^0 within the first hour of sputtering, which is consistent with the previous results using 1.5 eV/Ar. In addition, the N 1s spectra remain unchanged within 60 min (Figure 2c). Plotting the atomic ratio of C_P 1s to N1s in Figure 2d, one can see that after 10 min the ratio becomes constant, indicating a stable ratio between the remaining carbon and nitrogen. Simultaneously, the atomic ratio of I $3d_{5/2}$ to Pb 4f $_{7/2}$ in Figure 2e follows the same trend of C_P/N, indicating an initial loss of iodine, which then stabilizes after 10 min of sputtering. The evolution of I $3d_{5/2}$ with increased sputtering time can be seen in Figure S6 (Supporting Information). Furthermore, no argon implantation was detected using 1.5 eV/Ar as is evident in Figure S6 (Supporting Information).

In addition, the evolution of the work function and valence band within the first hour of sputtering is shown in **Figure 3a** and 3b, respectively. A nearly constant work function at 4.75 eV was observed upon increasing t_{GCIB} as has been previously reported above. It is worth mentioning that SPV measurements were conducted on the pristine sample with no noticeable change in the WF and VB, indicating flat band condition.[45] The valence band, however, exhibits an initial change in its features after 10 min and remains unaltered upon further exposure under 1.5 eV/Ar, following the same trend observed above. The slight shift by 0.16 eV toward lower kinetic energy of the SECO and higher binding energy of the VB main feature after 30 min in Figure 3 a and b can be attributed to the prolonged exposure to X-ray irradiation. X-ray exposure is found to induce a shift of perovskite energy levels toward higher binding energy by 0.16 eV, as shown in Figure S7 (Supporting Information). To disentangle the X-ray induced shift, an additional UPS measurement was performed on a fresh $MAPbI_3$ sample before and after GCIB sputtering at 1.5 eV/Ar without X-ray exposure, as presented in Figure 3d. The valence band onset clearly demonstrates a rigid shift toward higher binding energy by 0.22 eV after 10 min sputtering at 1.5 eV/Ar, accompanied by a slight change of the valence band structure. This can be ascribed to the modification of the surface stoichiometry, as seen from Figure 2. The reduction of contamination on the $MAPbI_3$ surface is likely linked to the removal of excess iodine and carbon. which aligns with the observed complete removal of C_{SC} and initial attenuation of iodine in Figure 2d, which stabilizes with continued sputtering. With a change in the stoichiometry at the surface after sputtering, changes in the energy levels of the clean $MAPbI_3$ are noted, revealing the intrinsic electronic properties of the perovskite surface. These residual components might originate from the use of

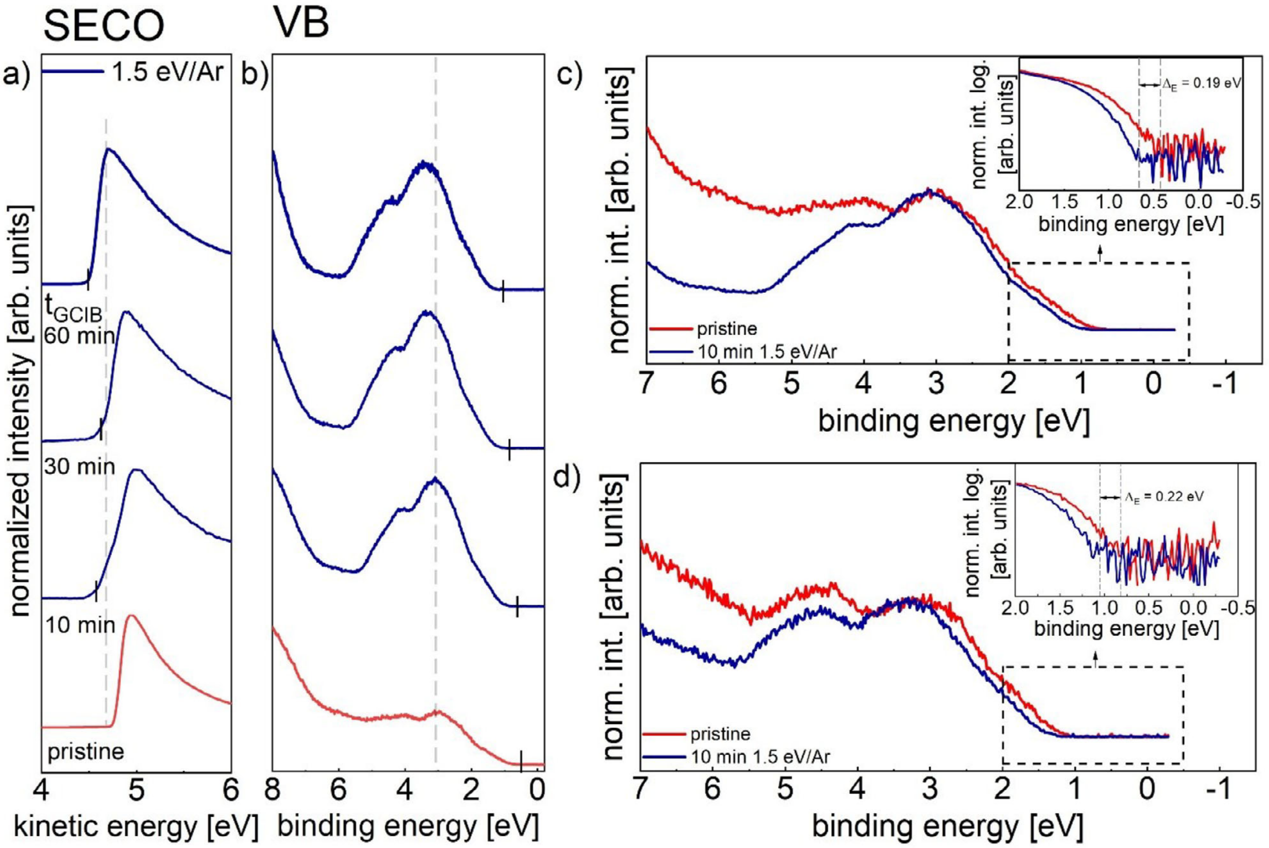

Figure 3. Evolution of a) SECO, b) valence band spectra of $MAPbI_3$ upon argon cluster cleaning at 1.5 eV/Ar. Detailed analysis of valence band spectra of the MAPbI3 sample before and after sputtering for 10 min under c) 1.5 eV/Ar and XPS exposure and d) 1.5 eV/Ar without XPS exposure normalized to the VB main feature at ca. 3 eV. Both insets in (c) and (d) are enlarged valence band spectra on a logarithmic intensity scale and normalized to the maximum intensity like the spectra in a) and b).

methylammonium-dimethyl sulfoxide during MHP film preparation which was reported to remain in the film and contribute to an additional density of states close to the VB onset[46] or the use of excess PbI_2, and consequently I_2, in the precursor solution to compensate for iodine loss under ultra-high vacuum condition. In strong contrast, exposing $MAPbI_3$ to single Ar ion beam already results in severe degradation after 10 min, with loss of the cation (Figure S9, Supporting Information) and a change of the VB structure (Figure S8, Supporting Information), similar to the degradation process observed under prolonged cluster sputtering.

Additional characterizations on morphology and optical properties of the $MAPbI_3$ samples after 1 h of sputtering under 1.5 eV/Ar present unchanged topography and absorption onset as compared to that of the pristine sample, as detailed in S10 and Figures S11 (Supporting Information). Thus, the use of GCIB at 1.5 eV/Ar for surface cleaning proves feasible without considerable degrading the perovskite films.

2.3. Impact of Surface Cleaning on Energy Level Alignment

Given the shift of the VB onset at the perovskite surface after 10 min of sputtering with 1.5 eV/Ar, the impact of surface cleaning on the energy level alignment at an exemplary perovskite/charge transport layer interface was investigated. To this end, thickness dependent UPS measurements of C_{60} molecules on pristine and Ar cluster cleaned $MAPbI_3$ films were conducted, respectively, as shown in Figure S12 (Supporting Information). The surface cleaning of $MAPbI_3$ film was conducted by GCIB sputtering under 1.5 eV/Ar for 10 min before C_{60} deposition.

In both cases, we find nearly identical evolution of the work function and highest occupied molecular orbital (HOMO) levels of C_{60} molecules upon increasing thickness, exhibiting essentially vacuum level alignment scenario at $MAPbI_3/C_{60}$ interface, i.e., the sample work function and HOMO-level position of C_{60} remain unchanged upon increasing the molecular layer thickness for both cases. The key electronic parameters are thus denoted in the energy level diagrams in **Figure 4**, which display nearly the same level alignment at the $MAPbI_3/C_{60}$ interface for both cases. However, it is worth noting that the valence band onset increases by 0.22 eV following Ar cluster sputtering on the perovskite surface, indicating the intrinsic valence band onset of the $MAPbI_3$ film (Figure 3d). Due to the surface cleaning, a potential enhancement in the device performance can be expected due to the elimination of the trap states and therefore reduced trap-assisted recombination.[41,47,48] Overall, the energy level diagram highlights the significance of the removal of

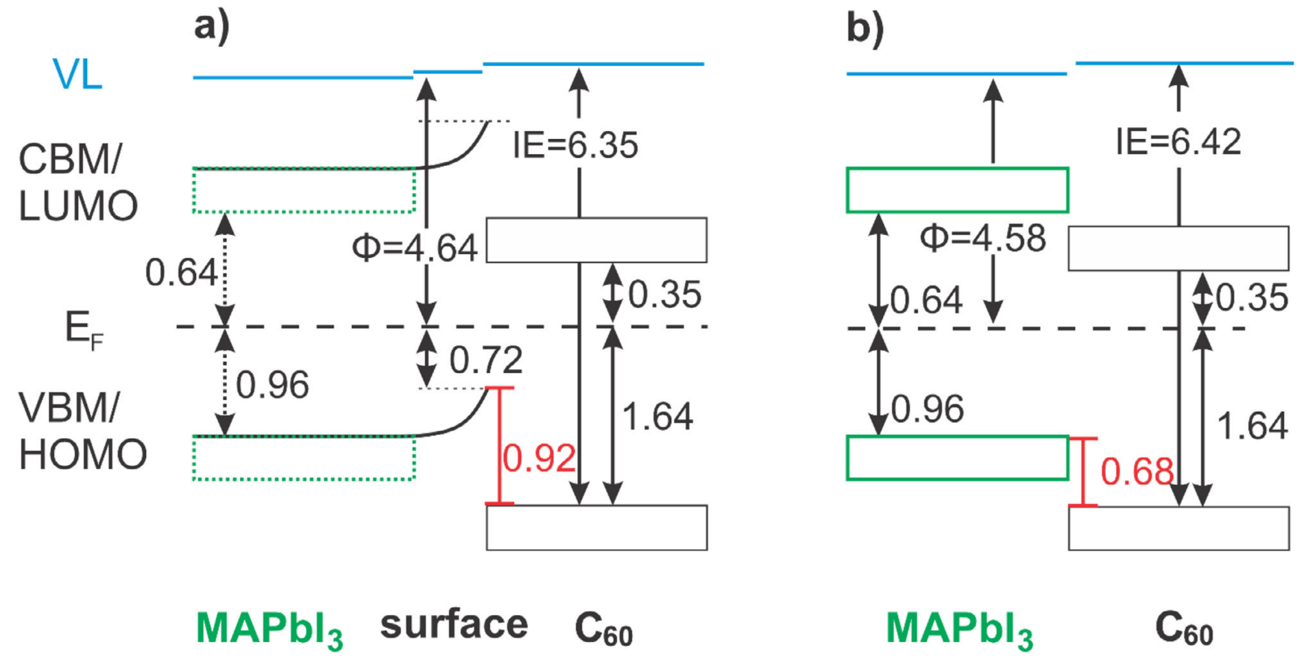

Figure 4. Energy level diagram of the C_{60}/$MAPbI_3$ interface without (a) and with (b) surface cleaning. All values are given in units of eV. The perovskite obtained after surface cleaning is considered to represent the intrinsic surface while the surface measured for the reference sample in a) includes the surface which induces band bending. The energy level of $MAPbI_3$ in b) is assumed to be the same as in a) since both samples have the same initial electronic parameters. The C_{60} lowest unoccupied molecular orbital (LUMO) was obtained by the reported electronic bandgap of 2.30 eV,[49, 50] For $MAPbI_3$ the position of the conduction band minimum (CBM) was determined by using the electronic bandgap which is identical to the optical bandgap due to low excitonic binding energy.[51] The optical bandgap of 1.60 eV was calculated using a Tauc plot (Figure S13, Supporting Information) and agrees with previous reports,[52, 53] VL denotes the vacuum level and Φ the work function.

a contaminated surface on the electronic properties of $MAPbI_3$, which is crucial for the investigation and tailoring of energy level alignment at perovskite surfaces and interfaces. Understanding the intrinsic electronic properties is of high relevance in further advancing the device performance, particularly given that surface contamination has already been shown to introduce uncontrollable variability, thereby hindering the reproducibility and comparability of the electronic characteristics of $MAPbI_3$ thin films.

3. Conclusion

We demonstrate the significant impact of using Ar-based GCIB sputtering on the electronic and chemical properties of $MAPbI_3$ films, revealed by photoemission spectroscopy. Long-term exposure to Ar clusters, necessary for depth profiling due to the low sputtering rate, leads to clear degradation at both 3.2 and 1.5 eV/Ar, characterized by a significant loss of cations and iodine and the emergence of a substantial amount of PbI_2 and Pb^0. This also evidences the fact that prolonged GCIB sputtering accelerates the degradation process of MAPbI3 in UHV conditions. The rate of sample degradation largely depends on the kinetic energy of the Ar clusters, with rapid degradation (after 1 h of exposure) observed under 3.2 eV/Ar. In contrast, short-term exposure of $MAPbI_3$ (within 1 h) to 1.5 eV/Ar reduces carbon contamination and excess iodine at the surface, without noticeable degrading the $MAPbI_3$ film. This gentle surface cleaning process reveals the intrinsic electronic structure at the surface, which differs from that with contamination by 0.22 eV. The reduction of contamination at the MAPbI3 surface enables the measurement of the intrinsic valence band and is expected to enhance the device performance by reducing trap-assisted non-radiative recombination. Thus, the use of GCIB sputtering could be used as a nondestructive surface treatment to reduce surface contamination for other MHP systems, potentially offering a method to reduce unpredictable surface components and therefore enhance reproducibility.

4. Experimental Section

Sample Preparation: The perovskite precursor solution for film fabrication was prepared under nitrogen atmosphere by dissolving 159 mg methylammonium iodide (MAI) (Dyenamo AB, 99.99% purity on trace elements basis) and 461 mg PbI_2 (Tokyo Chemical Industry 99.99% purity in trace metals basis, >98.0% total purity) in 71 µL dimethyl sulfoxide (DMSO, Sigma-Aldrich, ≥99.9% purity, anhydrous) and 0.6 mL of N,N dimethylformamide (DMF, Sigma-Aldrich, 99.8% purity, anhydrous) by mixing for ≈12 h. As substrates, we utilized quartz glass coated with indium tin oxide (ITO), cleaned with isopropanol and ethanol for 10 min each in the ultrasonic bath. After drying the substrate with N_2 gas and exposing each to (UV)-ozone for 15 min, the samples were directly introduced into a nitrogen-filled glove boxfor perovskite deposition.

The $MAPbI_3$ thin films were fabricated by spin-coating 40 µL of the precursor solution for 30 s at 4000 rpm on the cleaned ITO. After 10 s in the spin-coating process, 200 µL ethyl acetate (EA, Sigma-Aldrich, 99.8% purity, anhydrous) as the anti-solvent was introduced on top of the film. The crystallization was induced by annealing the sample for 3 min at 100 °C.

For the fabrication of a PbI_2 reference film, 461 mg of PbI_2 was dissolved in 1 mL DMF and mixed for ≈12 h. The solution was then heated at 80 °C for 2 h and while still hot, spin coated for 30 s at 6000 rpm on an ITO sample which was cleaned as described above.

All solutions were prepared one day before each film preparation and measurement. While the samples were prepared in a glove box with a nitrogen atmosphere, the samples were exposed to ambient air for a short time (5 min) before introducing into the photoemission system.

Photoemission Spectroscopy: All photoemission measurements were conducted under ultrahigh vacuum (UHV) and room temperature with a hemispherical analyzer EA15 using a microchannel plate (PREVAC). The UHV system is equipped with a monochromatic He I source with photon energy $h\nu = 21.22$ eV, and a monochromatic Al Kα x-ray source with $h\nu = 1486.6$ eV. Measurements of the SECO were performed with the application of a – 10.0 V sample bias. The calibration of the photoemission system was done by setting the Au Fermi edge for UPS and Au $4f_{7/2}$ for XPS of a clean single crystal Au(111) to 0 eV and 84 eV binding energy, respectively.

GCIB: Gas cluster ion beam sputtering was performed utilizing the GCIB 10S (Ionoptika), which allows the change of cluster size and energy selection. Here, two settings for achieving the lowest energy per argon atom E_{kin}/n (≈3000 Ar atoms with an acceleration voltage of 5 and 10 kV, respectively) were utilized with the maximal sputter area of 67.1 mm^2. The cluster beam of this setup can be represented by a 2D Gaussian function in x and y direction,

$$f(x,y) = \pi \cdot \sigma^2 \cdot e^{\frac{-(x^2+y^2)}{\sigma^2}} \tag{1}$$

with $\sigma = 0.3$ mm being the width of the cluster beam. The Ar cluster size distribution as a function of kinetic energy is shown in Supplementary Figure S1 (Supporting Information). The peak maximum of the distribution is taken to determine the kinetic energies per argon atom (E_{kin}/Ar) value. Both energy settings utilized show a good approximation of a Gaussian distribution of the cluster size with different full widths at half maxima of 3000 and 1700 atoms for 1.5 and 3.2 eV/Ar respectively. The difference in full width at half maximum is a direct result of the energy dependent formation of the clusters and gives rise to an uncertainty of one standard deviation, i.e., 0.3 and 0.1 eV/Ar for the energy settings 1.5 eV/Ar atom and 3.2 eV/Ar atom respectively.

Spectra Analysis: All XPS spectra were processed using CasaXPS software. A Shirley background was applied, and peak fitting was performed using a numerical convolution of Lorentzian and Gaussian line shapes. No additional data treatment was required. Due to variations in the measured counts per second across different samples, UPS spectra were typically normalized to the maximum intensity of each individual spectrum. In specific cases, normalization to a defined spectral feature was more appropriate; such instances are indicated in the corresponding figure captions. To facilitate accurate work function determination, a sample bias of −10.0 V was applied during UPS measurements to resolve the SECO. Consequently, all kinetic energy values were corrected by subtracting 10 eV during data processing. UPS data analysis was conducted using Origin 2018.

Supporting Information

Supporting Information is available from the Wiley Online Library or from the author.

Acknowledgements

This work was funded in part by the Deutsche Forschungsgemeinschaft (DFG, German Research Foundation, Project number 423749265-SPP2196 “SURPRISE”).

Conflict of Interest

The authors declare no conflict of interest.

Data Availability Statement

The data that support the findings of this study are available from the corresponding author upon reasonable request.

Keywords

energy level alignment, gas cluster ion beams, interfacial, metal halide perovskites, photoelectron spectroscopy

Received: February 1, 2025
Revised: April 27, 2025
Published online: May 23, 2025

---

[1] T. Baikie, Y. Fang, J. M. Kadro, M. Schreyer, F. Wei, S. G. Mhaisalkar, M. Graetzel, T. J. White, *J. Mater. Chem. A* **2013**, *1*, 5628.
[2] N.-G. Park, *Mater. Today* **2015**, *18*, 65.
[3] D. Shi, V. Adinolfi, R. Comin, M. Yuan, E. Alarousu, A. Buin, Y. Chen, S. Hoogland, A. Rothenberger, K. Katsiev, Y. Losovyj, X. Zhang, P. A. Dowben, O. F. Mohammed, E. H. Sargent, O. M. Bakr, *Science* **2015**, *347*, 519.
[4] T. Ishihara, *J. Lumin.* **1994**, *60*, 269.
[5] K. Tanaka, T. Takahashi, T. Ban, T. Kondo, K. Uchida, N. Miura, *Solid State Commun.* **2003**, *127*, 619.
[6] H. Zhang, X. Ji, H. Yao, Q. Fan, B. Yu, J. Li, *Sol. Energy* **2022**, *233*, 421.
[7] A. Fakharuddin, M. K. Gangishetty, M. Abdi-Jalebi, S.-H. Chin, A. R. bin Mohd Yusoff, D. N. Congreve, W. Tress, F. Deschler, M. Vasilopoulou, H. J. Bolink, *Nat. Electron.* **2022**, *5*, 203.
[8] Y. Wang, M.-L. Gao, J.-L. Wu, X.-W. Zhang, *Chin. Phys. B* **2019**, *28*, 018502.
[9] P. Schulz, *ACS Energy Lett.* **2018**, *3*, 1287.
[10] S. Teale, M. Degani, B. Chen, E. H. Sargent, G. Grancini, *Nat. Energy* **2024**, *9*, 779.
[11] A. Al-Ashouri, A. Magomedov, M. Roß, M. Jost, M. Talaikis, G. Chistiakova, T. Bertram, J. A. Márquez, E. Köhnen, E. Kasparavicius, S. Levcenco, L. Gil-Escrig, C. J. Hages, R. Schlatmann, B. Rech, T. Malinauskas, T. Unold, C. A. Kaufmann, L. Korte, G. Niaura, V. Getautis, S. Albrecht, *Energy Environ. Sci.* **2019**, *12*, 3356.
[12] F. Zu, D. Shin, E. Gutierrez-Partida, M. Stolterfoht, P. Amsalem, N. Koch, *Adv. Mater. Interfaces* **2023**, *10*, 2300413.
[13] F. Zu, P. Amsalem, M. Ralaiarisoa, T. Schultz, R. Schlesinger, N. Koch, *ACS Appl. Mater. Interfaces* **2017**, *9*, 41546.
[14] J. Warby, F. Zu, S. Zeiske, E. Gutierrez-Partida, L. Frohloff, S. Kahmann, K. Frohna, E. Mosconi, E. Radicchi, F. Lang, S. Shah, F. Peña-Camargo, H. Hempel, T. Unold, N. Koch, A. Armin, F. De Angelis, S. D. Stranks, D. Neher, M. Stolterfoht, *Adv. Energy Mater.* **2022**, *12*, 2103567.
[15] Y. Zong, Y. Zhou, Y. Zhang, Z. Li, L. Zhang, M.-G. Ju, M. Chen, S. Pang, X. C. Zeng, N. P. Padture, *Chem* **2018**, *4*, 1404.
[16] J. Wu, J. Shi, Y. Li, H. Li, H. Wu, Y. Luo, D. Li, Q. Meng, *Adv. Energy Mater.* **2019**, *9*, 1901352.
[17] Q. Chen, H. Zhou, Y. Fang, A. Z. Stieg, T.-B. Song, H.-H. Wang, X. Xu, Y. Liu, S. Lu, J. You, P. Sun, J. McKay, M. S. Goorsky, Y. Yang, *Nat. Commun.* **2015**, *6*, 7269.
[18] L. Zhao, Q. Li, C.-H. Hou, S. Li, X. Yang, J. Wu, S. Zhang, Q. Hu, Y. Wang, Y. Zhang, Y. Jiang, S. Jia, J.-J. Shyue, T. P. Russell, Q. Gong, X. Hu, R. Zhu, *J. Am. Chem. Soc.* **2022**, *144*, 1700.
[19] X. Xiao, C. Bao, Y. Fang, J. Dai, B. R. Ecker, C. Wang, Y. Lin, S. Tang, Y. Liu, Y. Deng, X. Zheng, Y. Gao, X. C. Zeng, J. Huang, *Adv. Mater.* **2018**, *30*, 1705176.
[20] W. Kong, C. Zhao, J. Xing, Y. Zou, T. Huang, F. Li, J. Yang, W. Yu, C. Guo, *Sol. RRL* **2020**, *4*, 2000189.

[21] S. Chen, Y. Liu, X. Xiao, Z. Yu, Y. Deng, X. Dai, Z. Ni, J. Huang, *Joule* **2020**, *4*, 2661.

[22] M. Kedia, M. Rai, H. Phirke, C. A. Aranda, C. Das, V. Chirvony, S. Boehringer, M. Kot, M. M. Byranvand, J. I. Flege, A. Redinger, M. Saliba, *ACS Energy Lett.* **2023**, *8*, 2603.

[23] F. Zu, D. Shin, N. Koch, *Mater. Horiz.* **2022**, *9*, 17.

[24] S. Béchu, M. Ralaiarisoa, A. Etcheberry, P. Schulz, *Adv. Energy Mater.* **2020**, *10*, 1904007.

[25] I. S. Zhidkov, D. W. Boukhvalov, A. F. Akbulatov, L. A. Frolova, L. D. Finkelstein, A. I. Kukharenko, S. O. Cholakh, C.-C. Chueh, P. A. Troshin, E. Z. Kurmaev, *Nano Energy* **2021**, *79*, 105421

[26] I. Yamada, *Mater. Sci. Eng. R Rep.* **2001**, *34*, 231.

[27] N. Toyoda, I. Yamada, *IEEE Trans. Plasma Sci.* **2008**, *36*, 1471.

[28] N. Toyoda, J. Matsuo, I. Yamada, *Nucl. Instrum. Methods Phys. Res. Sect. B Beam Interact. Mater. At.* **2004**, *216*, 379.

[29] K. Kim, W. Jae Chung, J. Lim, K.-J. Lee, H.-H. Kim, T. Schultz, P. Amsalem, W.-K. Choi, H.-K. Kim, J.-P. Ahn, H. Lee, J. Yeob Lee, S. Park, Y. Yi, *Appl. Surf. Sci.* **2023**, *611*, 155753.

[30] A. A. Sutanto, P. Caprioglio, N. Drigo, Y. J. Hofstetter, I. Garcia-Benito, V. I. E. Queloz, D. Neher, M. K. Nazeeruddin, M. Stolterfoht, Y. Vaynzof, G. Grancini, *Chem* **2021**, *7*, 1903.

[31] C. Noël, S. Pescetelli, A. Agresti, A. Franquet, V. Spampinato, A. Felten, A. di Carlo, L. Houssiau, Y. Busby, *Materials* **2019**, *12*, 726.

[32] H.-Y. Chang, W.-C. Lin, P.-C. Chu, Y.-K. Wang, M. Sogo, S.-I. Iida, C.-J. Peng, T. Miyayama, *ACS Appl. Nano Mater.* **2022**, *5*, 4260.

[33] D. Kim, H. J. Jung, I. J. Park, B. W. Larson, S. P. Dunfield, C. Xiao, J. Kim, J. Tong, P. Boonmongkolras, S. G. Ji, F. Zhang, S. R. Pae, M. Kim, S. B. Kang, V. Dravid, J. J. Berry, J. Y. Kim, K. Zhu, D. H. Kim, B. Shin, *Science* **2020**, *368*, 155.

[34] S. Bae, S. Kim, S.-W. Lee, K. J. Cho, S. Park, S. Lee, Y. Kang, H.-S. Lee, D. Kim, *J. Phys. Chem. Lett.* **2016**, *7*, 3091.

[35] B. Conings, J. Drijkoningen, N. Gauquelin, A. Babayigit, J. D'Haen, L. D'Olieslaeger, A. Ethirajan, J. Verbeeck, J. Manca, E. Mosconi, F. D. Angelis, H.-G. Boyen, *Adv. Energy Mater.* **2015**, *5*, 1500477.

[36] X. Tang, M. Brandl, B. May, I. Levchuk, Y. Hou, M. Richter, H. Chen, S. Chen, S. Kahmann, A. Osvet, F. Maier, H.-P. Steinrück, R. Hock, G. J. Matt, C. J. Brabec, *J. Mater. Chem. A* **2016**, *4*, 15896.

[37] F. Zu, T. Schultz, C. M. Wolff, D. Shin, L. Frohloff, D. Neher, P. Amsalem, N. Koch, *RSC Adv.* **2020**, *10*, 17534.

[38] J. A. Christians, P. A. Miranda Herrera, P. V. Kamat, *J. Am. Chem. Soc.* **2015**, *137*, 1530.

[39] F.-S. Zu, P. Amsalem, I. Salzmann, R.-B. Wang, M. Ralaiarisoa, S. Kowarik, S. Duhm, N. Koch, *Adv. Opt. Mater.* **2017**, *5*, 1700139.

[40] G. Sadoughi, D. E. Starr, E. Handick, S. D. Stranks, M. Gorgoi, R. G. Wilks, M. Bär, H. J. Snaith, *ACS Appl. Mater. Interfaces* **2015**, *7*, 13440.

[41] D. Shin, D. Kang, J-.B. Lee, J-.H. Ahn, I-.W. Cho, M-.Y. Ryu, S. W. Cho, N. E. Jung, H. Lee, Y. Yi, *J. Phys. Chem. Lett.* **2017**, *8*, 5423.

[42] J. F. Galisteo-López, M. Anaya, M. E. Calvo, H. Míguez, *J. Phys. Chem. Lett.* **2015**, *6*, 2200.

[43] S. Wang, Y. Jiang, E. J. Juarez-Perez, L. K. Ono, Y. Qi, *Nat. Energy* **2016**, *2*, 16195.

[44] M.-C. Jung, Y. M. Lee, H.-K. Lee, J. Park, S. R. Raga, L. K. Ono, S. Wang, M. R. Leyden, B. D. Yu, S. Hong, Y. Qi, *Appl. Phys. Lett.* **2016**, *108*, 073901.

[45] F. Zu, C. M. Wolff, M. Ralaiarisoa, P. Amsalem, D. Neher, N. Koch, *ACS Appl. Mater. Interfaces* **2019**, *11*, 21578.

[46] F. Zhang, J. C. Hamill, Y. Loo, A. Kahn, *Adv. Mater.* **2020**, *32*, 2003482.

[47] M. Stolterfoht, P. Caprioglio, C. M. Wolff, J. A. Márquez, J. Nordmann, S. Zhang, D. Rothhardt, U. Hörmann, Y. Amir, A. Redinger, L. Kegelmann, F. Zu, S. Albrecht, N. Koch, T. Kirchartz, M. Saliba, T. Unold, D. Neher, *Energy Environ. Sci.* **2019**, *12*, 2778.

[48] J. Warby, F. Zu, S. Zeiske, E. Gutierrez-Partida, L. Frohloff, S. Kahmann, K. Frohna, E. Mosconi, E. Radicchi, F. Lang, S. Shah, F. Peña-Camargo, H. Hempel, T. Unold, N. Koch, A. Armin, F. De Angelis, S. D. Stranks, D. Neher, M. Stolterfoht, *Adv. Energy Mater.* **2022**, *12*, 2103567.

[49] R. Könenkamp, G. Priebe, B. Pietzak, *Phys. Rev. B* **1999**, *60*, 11804.

[50] P. Schulz, L. L. Whittaker-Brooks, B. A. MacLeod, D. C. Olson, Y. Loo, A. Kahn, *Adv. Mater. Interfaces* **2015**, *2*, 1400532.

[51] A. Miyata, A. Mitioglu, P. Plochocka, O. Portugall, J. T. W. Wang, S. D. Stranks, H. J. Snaith, R. J. Nicholas, *Nat. Phys.* **2015**, *11*, 582.

[52] Y. Yamada, T. Nakamura, M. Endo, A. Wakamiya, Y. Kanemitsu, *Appl. Phys. Express* **2014**, *7*, 032302.

[53] A. M. A. Leguy, P. Azarhoosh, M. I. Alonso, M. Campoy-Quiles, O. J. Weber, J. Yao, D. Bryant, M. T. Weller, J. Nelson, A. Walsh, M. van Schilfgaarde, P. R. F. Barnes, *Nanoscale* **2016**, *8*, 6317.